Two-fluid biasing simulations of the large plasma device

Dustin M. Fisher and Barrett N. Rogers
Department of Physics and Astronomy, Dartmouth College, Hanover, New Hampshire 03755, USA

(Received 28 September 2016; accepted 23 January 2017; published online 8 February 2017)

External biasing of the Large Plasma Device (LAPD) and its impact on plasma flows and turbulence are explored for the first time in 3D simulations using the Global Braginskii Solver code. Without external biasing, the LAPD plasma spontaneously rotates in the ion diamagnetic direction. The application of a positive bias increases the plasma rotation in the simulations, which show the emergence of a coherent Kelvin Helmholtz (KH) mode outside of the cathode edge with poloidal mode number $m \simeq 6$. Negative biasing reduces the rotation in the simulations, which exhibit KH turbulence modestly weaker than but otherwise similar to unbiased simulations. Biasing either way, but especially positively, forces the plasma potential inside the cathode edge to a spatially constant, KH-stable profile, leading to a more quiescent core plasma than the unbiased case. A moderate increase in plasma confinement and an associated steepening of the profiles are seen in the biasing runs. The simulations thus show that the application of external biasing can improve confinement while also driving a Kelvin-Helmholtz instability. Ion-neutral collisions have only a weak effect in the biased or unbiased simulations. *Published by AIP Publishing.*
[http://dx.doi.org/10.1063/1.4975616]

I. INTRODUCTION

Over the past decade, researchers have explored the effects of plasma biasing and its impact on flows and turbulence in the Large Plasma Device (LAPD).[1] Without external biasing, the LAPD plasma spontaneously rotates in the ion diamagnetic direction, expected theoretically and reproduced by our simulations as the plasma charges slightly positive to counterbalance the larger electron (than ion) thermal streaming particle losses along the magnetic field to the end walls. This creates a positive radial electric field and an associated $E \times B$ drift in the ion diamagnetic direction. This unbiased spontaneous rotation of the LAPD plasma can be modified through biasing to increase the rotation, nearly null it, or reverse it completely.[2] Numerous studies have shown biasing to be a mechanism for confinement as well as a means of controlling azimuthal sheared flow, which subsequently modifies the turbulent dynamics.[2–8]

Previous simulations of LAPD[9–14] have either focused on the unbiased regime or in the case of Friedman *et al.*[13] have modeled null-flow conditions that are relevant mainly to experiments that reduce or nearly null the intrinsic rotation through careful biasing.[8]

Building upon the study of the unbiased regime of LAPD by Fisher *et al.*,[14] we explore external biasing through boundary conditions that partially model the biasing configuration in LAPD. Two regimes are explored: positive bias that increases the intrinsic rotation in the ion-diamagnetic direction and negative bias that decreases the rotation or sometimes reverses it.

Early studies[3,5,6] biased the side walls of the vacuum vessel relative to the plasma source. Later work by Zhou *et al.*[7] used a copper obstacle in the plasma to drive sheared azimuthal flow. Of greatest relevance to this work, Schaffner *et al.*[2,8] improved biasing control with an iris-like limiter at the cathode end.

Our numerical model employs a simple limiter shape near the cathode-anode source end of the simulation domain that aims to partially model the experiments of Schaffner *et al.*,[8] in which an annular limiter near the cathode end of LAPD is biased with respect to the core plasma and anode. This limiter is encompassed by a second electrically isolated biasable annulus that terminates radially at the side walls and can be separately biased during experiments or left to float. For this study, we simplify this arrangement and consider the application of just a single non-zero wall bias within a circular zone encompassing the cathode with the chamber walls and elsewhere held at ground. This study therefore does not capture the complete bias dynamics in the experiments, in particular, the flows at the far edge of the LAPD generated when the various annular and wall potentials differ. These differences from the study by Schaffner *et al.*[8] can lead, at the least, to a shift in rotational reference frame.

Since the dilation of the limiter in the experiment determines the source front of electrons from the cathode, we choose the limiter bias profile to be the same as the plasma source profile in the simulations. We show a diagram of the biasing setup for both the LAPD and Global Braginskii Solver code (GBS) in Figure 1.

II. BIASING SETUP

The LAPD creates a linear plasma approximately 17 m in length and 30 cm in radius with an axially directed magnetic field. At one end is a barium-oxide cathode that thermionically emits electrons that are subsequently accelerated into the plasma chamber by a biasable anode mesh. At the far-end of the device, the plasma terminates on an end mesh that can be biased or left to float depending on the experiment. Under normal unbiased operating conditions, the plasma rotates in the ion-diamagnetic direction. We have

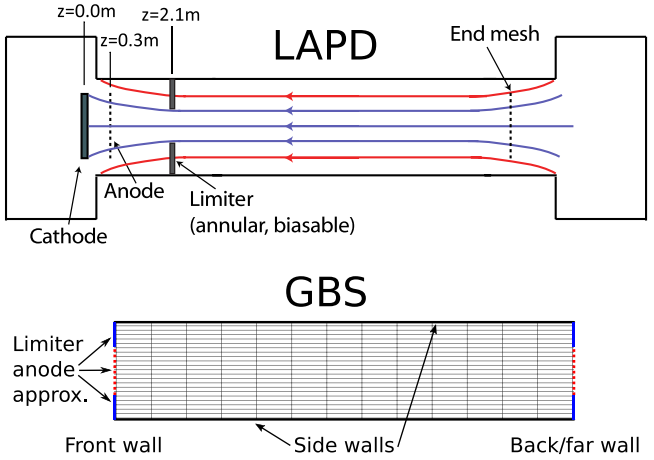

FIG. 1. Biasing schematics of LAPD and GBS. Reproduced with permission from Schaffner *et al.*, Phys. Plasmas **20**(5), 055907 (2013). Copyright 2013 AIP Publishing.

proposed that this unforced rotation is due to the mechanism mentioned earlier.[14]

Our simulations use a modified version of the 3D Global Braginskii Solver code (GBS), which we previously used to study turbulence and transport in the unbiased regime of LAPD.[9,14] Assuming $T_i \ll T_e$, the code evolves a set of five electrostatic two-fluid drift-reduced Braginskii equations[15]

$$\frac{dn}{dt} = -\frac{\partial(nV_{\|e})}{\partial z} + \mathcal{D}_n(n) + S_n, \tag{1}$$

$$\frac{d\omega}{dt} = -V_{\|i}\frac{\partial\omega}{\partial z} + \frac{m_i\Omega_{ci}^2}{e^2 n}\frac{\partial j_\|}{\partial z} - \nu_{in}\omega + S_\omega, \tag{2}$$

$$m_e\frac{dV_{\|e}}{dt} = -m_e V_{\|e}\frac{\partial V_{\|e}}{\partial z} + \frac{4}{3}\frac{\eta_{0e}}{n}\frac{\partial^2 V_{\|e}}{\partial z^2} + \frac{ej_\|}{\sigma_\|} + e\frac{\partial\phi}{\partial z} - \frac{T_e}{n}\frac{\partial n}{\partial z} - 1.71\frac{\partial T_e}{\partial z}, \tag{3}$$

$$m_i\frac{dV_{\|i}}{dt} = -m_i V_{\|i}\left(\frac{\partial V_{\|i}}{\partial z}\right) + \frac{4}{3}\frac{\eta_{0i}}{n}\frac{\partial^2 V_{\|i}}{\partial z^2} - \frac{1}{n}\frac{\partial p_e}{\partial z}, \tag{4}$$

$$\frac{dT_e}{dt} = -V_{\|e}\frac{\partial T_e}{\partial z} + \frac{2}{3}\frac{T_e}{en}0.71\frac{\partial j_\|}{\partial z} - \frac{2}{3}T_e\frac{\partial V_{\|e}}{\partial z} + \mathcal{D}_{T_e}^{\|}(T_e) + \mathcal{D}_{T_e}(T_e) + S_T, \tag{5}$$

where n is the plasma density, ϕ is the electrostatic potential evolved through the vorticity $\omega = \nabla_\perp^2\phi$, T_e is the electron temperature, $V_{\|e}$ and $V_{\|i}$ are the parallel electron and ion velocities, $p_e = nT_e$ is the electron scalar pressure, $df/dt = \partial f/\partial t - (c/B)[\phi, f]$ is the total time derivative with Poisson bracket $[A,B] = \partial_x A\partial_y B - \partial_y A\partial_x B$, $j_\| = en(V_{\|i} - V_{\|e})$ is the current density, $\sigma_\|$ is the parallel electrical conductivity, $\Omega_{ci} = eB/m_i c$ is the ion cyclotron frequency, ν_{in} is the ion-neutral collision rate, and η_{0i} and η_{0e} are the parallel ion and electron viscosities.

Sources for the density, temperature, and vorticity are represented as S_n, S_T, and S_ω and are described in further detail by Fisher *et al.*[14] The vorticity source represents the injection of electrons into the plasma by the anode. The vorticity equation represents the electric current continuity equation $\nabla\cdot\vec{j}_{\text{tot}} = 0$ and thus this injection must be included there. In unbiased and positively biased runs, this source has only a minor effect, while at negative bias the flows can become so weak that the vorticity source has a seemingly significant impact on the potential.

Eqs. (1)–(5) are solved on a field-aligned Cartesian grid parallel to z using a finite difference method with fourth-order Runge-Kutta time stepping and small numerical diffusion terms $\mathcal{D}^{\|}$ and $\mathcal{D}$. The grid size is $n_x = n_y = 256$, $n_z = 64$. The GBS normalization is based on the reference parameters for a He plasma: $T_{e0} = 6\,\text{eV}$, $n_0 = 2\times10^{12}\text{cm}^{-3}$, $\Omega_{ci} = eB/m_i c \sim 150$ kHz, $c_{s0} = \sqrt{T_{e0}/m_i} \sim 1.2\times10^6$ cm/s, and $\rho_{s0} = c_{s0}/\Omega_{ci} \sim 1.25$ cm.

The side walls in the simulations perpendicular to the magnetic field span $-L/2$ to $L/2$ where $L = 100\rho_{s0}$ is the domain width. This width is somewhat larger than the actual LAPD diameter so that essentially all the plasma is lost in the parallel direction before reaching the side walls of the simulations. The parallel domain spans $-L_z/2$ to $L_z/2$ where $L_z = 36R$ and is normalized to the LAPD radius $R = 0.5$ m. The cathode (sourced) end is at negative z. Perpendicular scales are normalized to the reference ion-sound gyroradius ρ_{s0} and parallel scales to the machine radius R. As in our numerical simulations of LAPD in the unbiased regime,[14] we use an ion neutral collision rate $\nu_{in}/\omega_{ci} = 1\times10^{-3}$ which is consistent with a neutral density of $n_n \sim 10^{11}\text{cm}^{-3}$.[5,11]

Bohm sheath boundary conditions are applied at the front and end walls along the magnetic field

$$V_{\|i} = \pm c_s, \tag{6}$$

$$V_{\|e} = \pm c_s\exp\left([\Lambda - e\{\phi - \phi_{\text{wall}}\}/T_e]\right), \tag{7}$$

where c_s is the ion sound speed, $\Lambda = \ln\sqrt{m_i/(2\pi m_e)} \simeq 3$ is the sheath factor, ϕ is the plasma potential, and ϕ_{wall} is now included as a biasing profile applied to one or both of the end-walls. An inner radial region of the front (cathode end) wall is biased relative to the side walls using

$$\phi_{\text{wall}} = \phi_{\text{bias}}\{1 - \tanh[(r - r_{\text{lim}})/L_{\text{lim}}]\}, \tag{8}$$

where ϕ_{bias} is the desired potential difference between the limiter and the plasma and the limiter radius r_{lim} and profile scale length L_{lim} models the plasma source profiles. The far wall opposite to the cathode (positive z) can be grounded to mimic the target LAPD configuration or biased the same way as the front wall, allowing us to explore the role of axial variation.

The wall bias ϕ_{wall} enters the simulations through the parallel sheath boundary conditions alone. Its biggest impact on the plasma potential occurs through the $\partial_z j_\|$ term in the vorticity equation and, in particular, the tendency of the simulations to seek a quasi-equilibrium state in which $\partial_z j_\|$ is small, driving $V_{\|e} \to V_{\|i}$. In the double wall biasing simulations discussed later in which ϕ_{wall} is the same at both ends along z, the axial variation of ϕ is weak, and this condition leads to approximately $\phi \simeq \phi_{\text{wall}} + \Lambda T_e/e$ (the residual terms in the vorticity equations such as the vorticity source and the Reynolds stress can be incorporated into a

redefinition $\Lambda \rightarrow \Lambda'$ discussed below). In the unbiased case that $\phi_{\text{wall}} = 0$ on both ends, this reduces to $\phi \simeq \Lambda T_e/e$, consistent with the spontaneous $E \times B$ rotation of the plasma in the ion diamagnetic direction (in the case of the ion diamagnetic drift $e\nabla\phi = \Lambda\nabla T_e \rightarrow (1/n)\nabla p_i$). In the single wall biasing simulations that are relevant to LAPD in which ϕ_{wall} is nontrivial on the cathode end while $\phi_{\text{wall}} = 0$ at the opposite end, the relationship of ϕ to the applied one-wall bias is not so clear. We show later that such a quasi-2D estimate applies very roughly only in the positively biased simulations, in which the electrons preferentially stream into the positively biased cathode end rather than the opposite, grounded wall, off-setting both the ion outflows and the inward injection of electrons represented by the vorticity source.

We present 3D GBS simulations of the LAPD for the unbiased baseline configuration and the negatively and positively biased one-wall and two-wall cases. Biasing both walls, though not directly relevant to LAPD, minimizes axial potential variation and establishes contact with the 2D limit, simulations of which we also present. For single- and double-wall positive biasing runs, the wall potential is ramped up to $\phi_{\text{bias}} = 24$ V, which we represent in GBS normalized units as $\phi_{\text{bias}} = +4$, where $\phi = e\phi_{\text{phys}}/T_{e0}$ is the normalized GBS plasma potential and $T_{e0} = 6$ eV is the reference temperature. A negative wall bias may also be applied to oppose the unbiased flow. For single- and double-wall negative biasing runs, we choose the negative wall bias $\phi_{\text{bias}} = -18$ V, corresponding to normalized $\phi_{\text{bias}} = -3$. Typical LAPD discharges pulse the plasma on the order of 1 Hz with each pulse lasting about 10 ms and biasing occurring a few milliseconds into the run. This is modeled in the simulations by introducing biasing about 1.5 ms after the plasma becomes turbulent and smoothly ramping the bias from zero to the desired value over a few hundred microseconds, comparable with voltage rise times in LAPD.

Figures 2 and 3 show a four-point radial average of the density versus time at various locations in the simulation domain for the positive and negative biasing simulations. For both biasing regimes, fluctuations reach the radial location of the LAPD machine edge (smaller than the simulation edge) in the simulation at 0.5 m about 2 ms into the run (shown for instance in Figure 2(c)). While it is difficult to discern changes in the plasma fluctuations in the negative case shown in Fig. 3 from the pre-biased fluctuations (indicative of the similarity of these cases discussed later), Fig. 2 shows a strongly increased fluctuation frequency from pre-biased values. As we will explain, the application of biasing to only a single end (rather than both) has a potentially much larger impact on the plasma potential in the positively biased case.

When axial variation is sufficiently slow and finite $k_\parallel$ modes are unimportant, the Braginskii equations can be integrated over z to yield a set of approximate 2D fluid equations[9] we simulate later

$$\frac{dn}{dt} = -\sigma\frac{nC_s}{R}\exp(\Lambda - e\Delta\phi/T_e) + \mathcal{S}_n, \quad \sigma = 1.5\frac{R}{L_z}, \tag{9}$$

$$\frac{d\nabla^2\phi}{dt} = \sigma\frac{C_s m_i\omega_{ci}^2}{eR}[1 - \exp(\Lambda - e\Delta\phi/T_e) + \mathcal{S}_\omega - \nu_{in}\omega], \tag{10}$$

$$\frac{dT_e}{dt} = -\sigma\frac{2T_eC_s}{3R}[1.71\exp(\Lambda - e\Delta\phi/T_e) - 0.71] + \mathcal{S}_T, \tag{11}$$

where $\Delta\phi = \phi - \phi_{\text{wall}}$, L_z is the axial length of the plasma, and the factor 1.5 is an axial sheath drop rate from the 3D runs that approximates the density drop leading into the

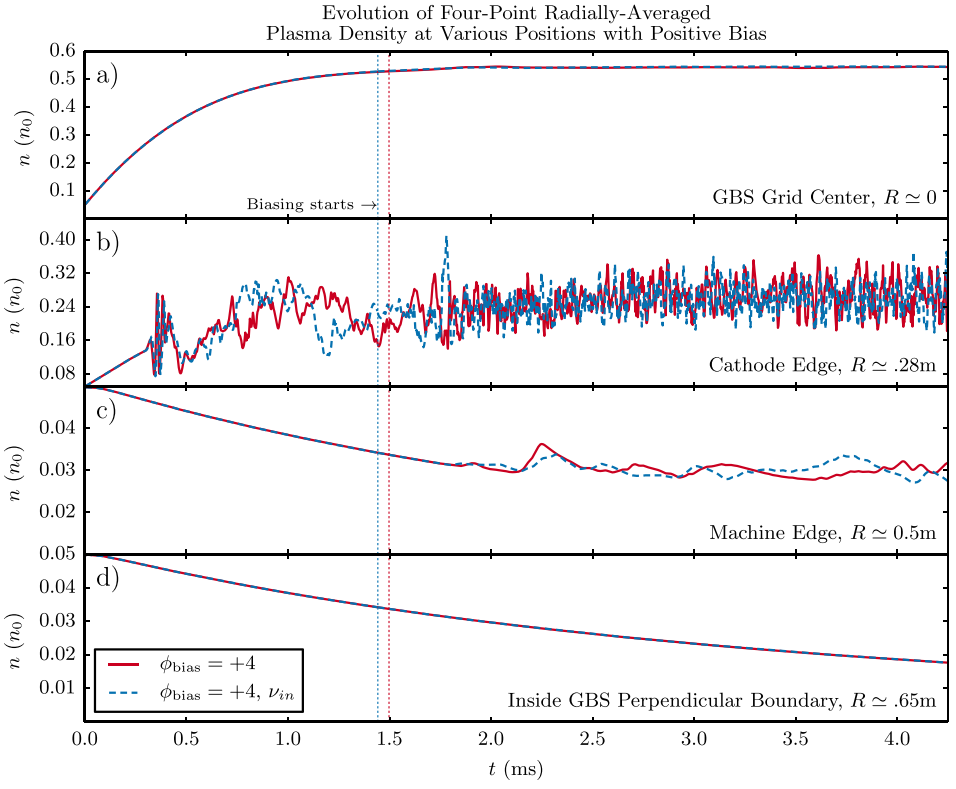

FIG. 2. Midplane density values averaged at four radial points as a function of time for $\phi_{\text{bias}} = +4$ both with (dotted line) and without (solid line) ion-neutral collisions, ν_{in}. (a) at the center of the simulation; (b) at the limiter/cathode edge; (c) at the location of the machine edge in LAPD; and (d) near the boundary of the GBS radial domain.

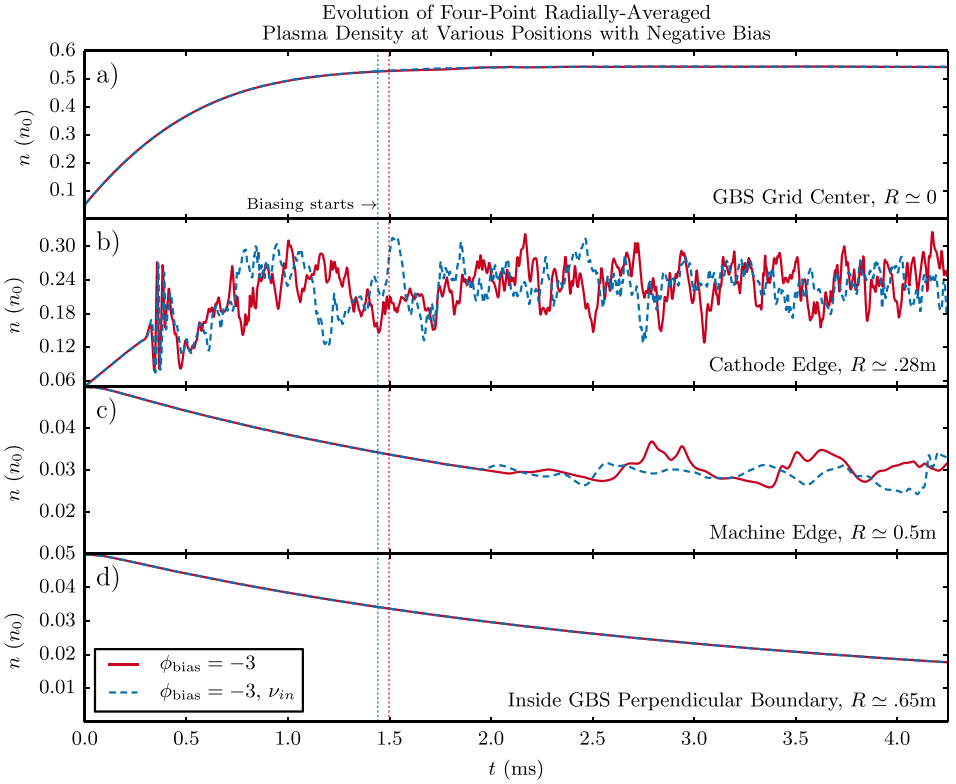

FIG. 3. Midplane density values averaged at four radial points as a function of time for $\phi_{\text{bias}} = -3$ both with (dotted line) and without (solid line) ion-neutral collisions, ν_{in}. (a) at the center of the simulation; (b) at the limiter/cathode edge; (c) at the location of the LAPD machine edge; and (d) near the boundary of the GBS radial domain.

sheath edge. Eqs. (9)–(11) are evolved using a 2D version of GBS with the same reference parameters and perpendicular computational domain as the 3D runs. Following Fisher *et al.*[14] the time-averaged potential can then be estimated in quasi-2D configurations through the modified sheath parameter Λ' and the equilibrium electron temperature as well as the corresponding time-averaged local sound speed

$$\langle\phi\rangle \simeq \phi_{\text{wall}} + \Lambda'\langle T_e\rangle \tag{12}$$

with

$$\Lambda' = \Lambda - \ln(G), \tag{13}$$

$$G = 1 + \frac{L_z}{(f_{\text{ce}} + f_{\text{fe}})}\frac{1}{\langle C_s\rangle}\left[\mathcal{S}_\omega + \langle\mathcal{D}_\omega(\omega)\rangle - \frac{R}{\rho_{s0}}(\langle[\delta\phi, \delta\omega]\rangle + \nu_{in}\langle\omega\rangle)\right]. \tag{14}$$

Here, $\Lambda \simeq 3$ is the Bohm sheath parameter, f_{ce} and f_{fe} are the axial density sheath drop estimates at the cathode edge and far edge, C_s is the local sound speed, and $\mathcal{D}_\omega(\omega)$ is a second order diffusion operator, which makes a negligible contribution here.

All time-averaged values (unless otherwise stated) are computed over a time window of 2 ms in the quasi-steady state phase. This window is similar to that used with LAPD biasing data and appropriately allows for multiple eddy-turnover times. Moreover, it is larger by at least a factor of 2 than the autocorrelation times τ_{ac}, approximated here by comparing various time-averaged windows. (The autocorrelation time is a measure of the convergence rate of an ergodic data set to its mean and is non-trivial to calculate from data.[16]) The density sheath drop rates are a measure of the average drop in density from the maximum to the sheath edge. There is radial variation in these terms, but this has little effect on the shape of the estimated potential. Estimates of $f_{\text{ce}} + f_{\text{fe}}$ are on the order of 1.8, comparable to the value 3/2 used in previous work.[9]

It has been suggested[5] that the plasma rotation in LAPD is due to the $J \times B$ torque from ion-neutral collisions entering though the Pedersen conductivity. In our simulations, ν_{in} enters through damping terms $\propto\nu_{in}$ on the right sides of the vorticity equations; in our simulations they have only a small impact, such as in the time-averaged potential plots of Fig. 4. The nonlinear Reynolds stress has also been proposed as a possible mechanism for plasma rotation.[17] The Reynolds stress, shown in Fig. 5, is a nonlinear term that convects momentum in the vorticity equation. In our analysis it can be incorporated into Λ' (the $\langle[\delta\phi, \delta\omega]\rangle$ term) and also has a small effect on the plasma potential in all cases.

III. BIASING RESULTS

The quasi-2D assumption is at least roughly applicable in all but the single wall negatively biased case, in which the axial variation of the potential is nontrivial. Aside from that case, the $E \times B$ rotation of the simulations is approximately described by $\phi = \phi_{\text{wall}} + \Lambda' T_e$. Figs. 6 and 7 show the time-averaged electric potential $\langle\phi\rangle$, the estimate given by Eq. (13), and the applied wall biases. The estimated potentials in Figs. 6(b) and 7(b) show good agreement in the case that both the front and far walls are equally biased, and rough agreement with the positively biased single wall simulation in Fig. 7(a). But the estimate $\phi = \phi_{\text{wall}} + \Lambda' T_e$ clearly fails in the negatively biased single wall simulation shown in Fig. 6(a). The potential in this case, shown in Fig. 8, matches $\phi \simeq \Lambda' T_e$ at the far (positive z) grounded wall where $\phi_{\text{wall}} = 0$ and

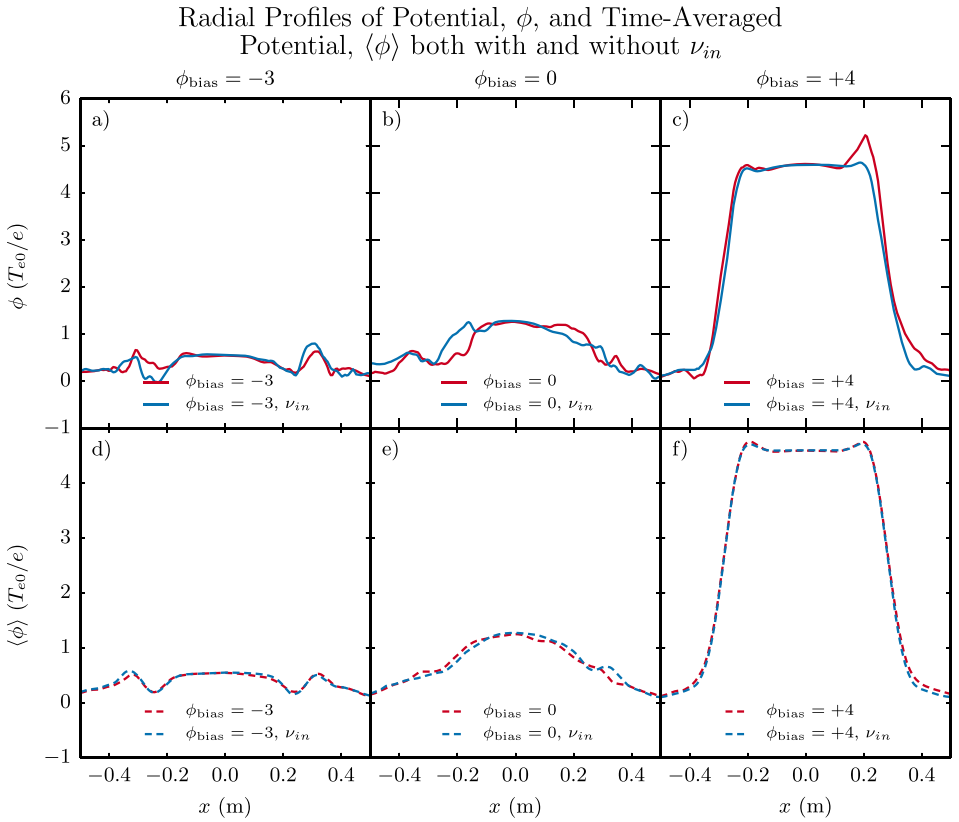

FIG. 4. Midplane potential profiles comparing biasing runs (left and right columns) to the unbiased low-flow regime (center column). Total potential profiles are shown in the top row, while time-averaged equilibrium quantities are shown in the bottom row.

drops axially to values near zero at the negatively biased cathode end, well short of $\phi_{wall} = -3$ there. The potential shows strong perpendicular variation near the cathode edge, where the biasing is attempting with little success to reverse the flow in the electron diamagnetic direction.

Given the boundary condition 7, the application of a front wall bias substantially below $-\Lambda T_e/e$ leads to $V_{\|e} \simeq 0$ (the electrons being fully repulsed by a negatively biased wall), after which further reduction of ϕ_{wall} has no effect on the plasma. All of the electrons preferentially flow along the field into the far-end, grounded wall (the parallel flows are shown later). In other words, the application of a negative bias to a single wall substantially below $-\Lambda T_e/e$ cannot, in the presence of a grounded far-end wall, substantially lower $e\phi_{\rm phys}/T_e$ below zero.

In contrast, the positively biased plasma potential shown in Fig. 9 is set mainly by the front wall through the relation $\phi = \phi_{\rm wall} + \Lambda' T_e$ and remains approximately at this level

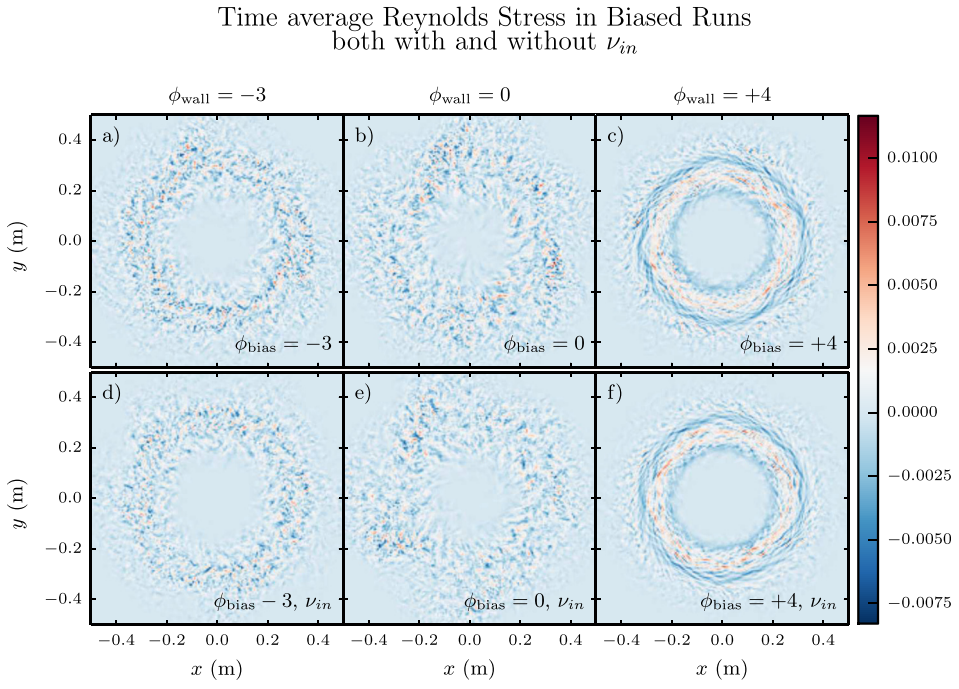

FIG. 5. Time-averaged Reynolds stress from the nonlinear convective term in the vorticity equation, $\langle[\delta\phi, \delta\omega]\rangle$ both with and without ion-neutral collisions, ν_{in}. Units are GBS normalized.

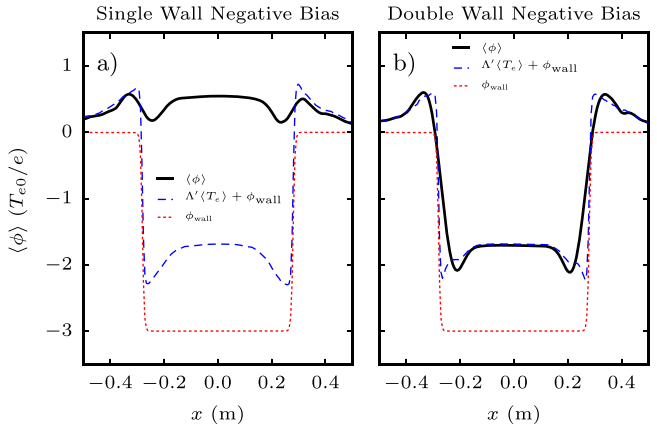

FIG. 6. Comparison of time-averaged potential profiles between (a) single and (b) double wall biasing with $\phi_{\rm bias} = -3$. The expected potential from the modified sheath factor, Λ', is shown in each instance along side the biased wall potential profile.

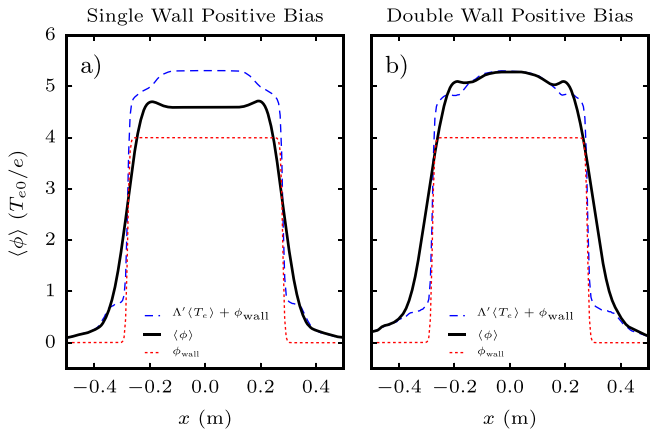

FIG. 7. Comparison of time-averaged potential profiles between (a) single and (b) double wall biasing with $\phi_{\rm bias} = +4$. The expected potential from the modified sheath factor, Λ', is shown in each instance along side the biased wall potential profile.

along the entire z domain. The electrons now flow predominantly into the positively biased wall compared to the grounded far wall. The weak axial variation of the potential in this case is required by the parallel electron momentum equation (3), which would otherwise exhibit an unacceptably large parallel electric field ($E_z = -\partial_z\phi$) that would drive electron flows inconsistent with the $V_{\|e}$ boundary conditions. The parallel gradients $\partial_z n$, $\partial_z T_e$ are similarly limited. Thus, the positively biased one wall simulation is roughly quasi-2D.

Focusing now on the single-wall biasing runs, Figs. 10–14 show midplane cross-sectional snapshots of the density, temperature, potential, and parallel electron and ion velocities for each biasing regime. The fluctuations in the plots are driven (as we will demonstrate) by $k_\| = 0$ Kelvin-Helmholtz (KH) instabilities. As expected, the parallel electron flow is positively skewed at negative bias and negatively skewed at positive bias. The structure of the KH-induced fluctuations in the unbiased and single wall negatively biased cases is roughly similar, which reflects the similarity of the potential in the negatively biased run (Fig. 8) to a moderately weakened, negatively shifted and axially varying version of the unbiased plasma potential (Fig. 4(e)). The potential in the positively biased case is very flat inside the cathode edge, mostly suppressing rotation and KH activity there.

In such cases where the plasma potential assumes an approximate top-hat shape, the associated poloidal $E \times B$ flow profile $V_{E\theta} = -(c/B)\partial_r\phi_{\rm phys}$ represents a radially sheared jet of plasma with fixed $\Delta\phi = \int \partial_r\phi dr \propto V_{E\theta}\delta$ where $\Delta\phi$ is the applied bias voltage and $V_{E\theta}$ and δ are the average velocity and radial width of the jet. The width δ in all our simulations is significantly larger than that of the applied bias function $\phi_{\rm wall}$ and is governed by the KH-driven transport across the sheared layer, with weaker transport

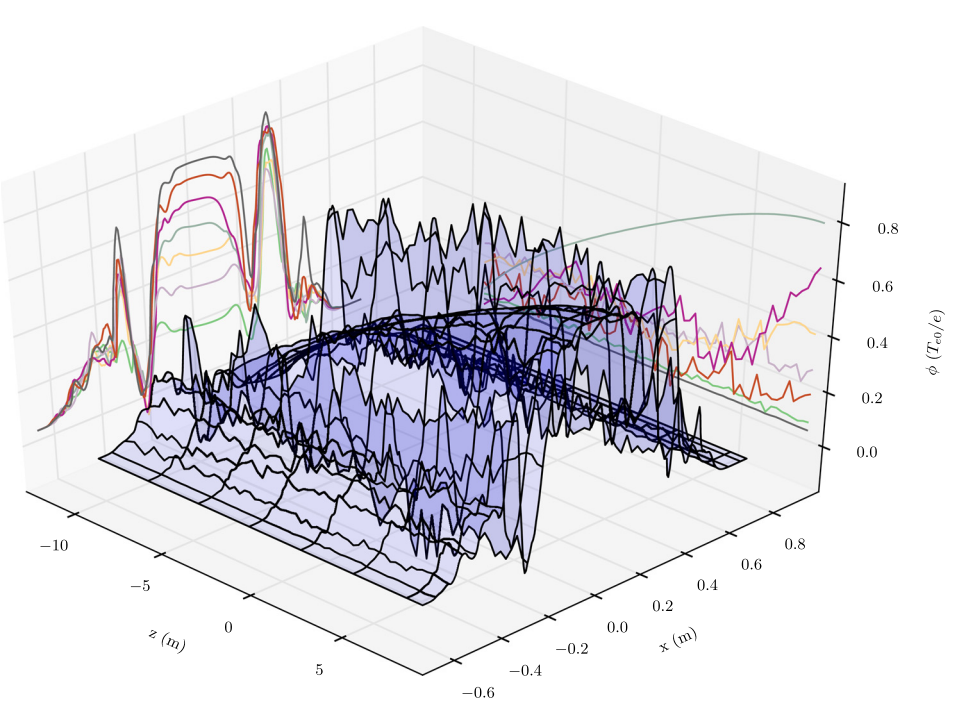

FIG. 8. Midplane electric potential as a function of axial position in the case where $\phi_{\rm wall} = -3$. Projected contour lines show the drop in plasma potential in response to end-wall sheath boundary conditions.

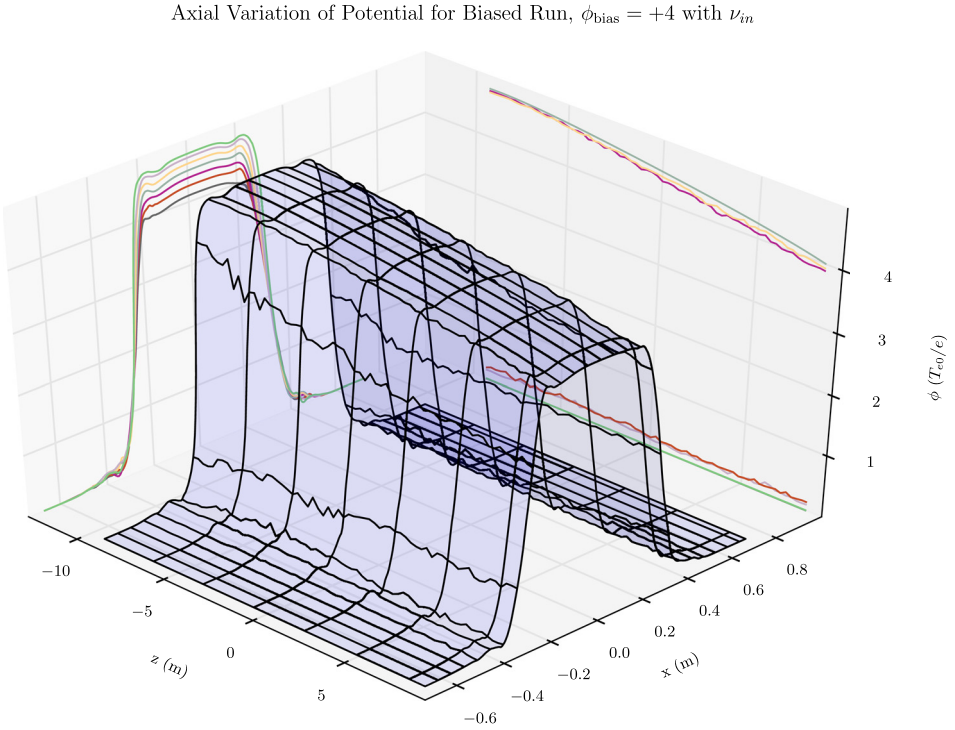

FIG. 9. Midplane electric potential as a function of axial position in the case where $\phi_{\text{wall}} = +4$. Projected contour lines show the drop in plasma potential in response to end-wall sheath boundary conditions.

leading to narrower layers, steeper plasma profiles, and faster peak poloidal $E \times B$ velocities.

Radial profiles of the density and corresponding time averages are shown in Figs. 15 and 16. Both biased average density profiles show moderate steepening and improved central confinement. The plateaus in the positively biased average density reflect the saturated quasi-coherent mode with poloidal mode number $m \simeq 6$ visible as an inner and outer hexagonal ring of vortices in Figs. 10–12. The poloidal $E \times B$ velocity profile associated with the positively biased potential of Fig. 9 is approximately zero in the regions inside the cathode edge and well outside, separated by a uni-directional jet in the ion diamagnetic direction (clockwise here). As such, it corresponds roughly to inner negative and outer positive vortex sheets, which nonlinearly produce the vortex rings. The central flatness of the positively biased average density in Fig. 15(f), indicative of good particle confinement, shows that the saturated KH mode, while presumably an effective means of vorticity transport and dissipation, produces relatively weak particle transport. This illustrates a significant finding of this work: increasing the bias, while destabilizing KH modes, leads to overall better plasma confinement in the simulations.

Turning to the parallel structure, cuts along z parallel to the magnetic field are shown in Figs. 17 and 18. To highlight the fluctuations, corresponding plots of the temperature, density, and potential with the time-averages subtracted off are shown in Figs. 19 and 20. The latter illustrate the predominantly $k_{\parallel} = 0$ nature of the fluctuations, consistent with KH modes and inconsistent with driftwaves, which require finite $k_{\parallel}$ to be unstable. The parallel flow of electrons in the negatively biased case, as expected, is near zero at the (strongly repulsive) cathode end, and positive at the far, grounded end. This net outflow counterbalances the ion outflow and the input of electrons by the anode, entering the model through the vorticity source.

Figure 21 shows midplane cuts of the density fluctuations and spectral power density over a window of 2 ms in the quasi-equilibrium region of both the unbiased and biased runs. The fluctuation profile in the negatively biased simulation is about ∼15% weaker than the unbiased run and similar in shape, consistent with the rough similarity of the potential profiles. The positively biased profile shows a strong peak at the cathode edge (marked by vertical dotted lines) due to the quasi-coherent mode, with reduced fluctuations relative to the unbiased case both in the core and a few centimeters

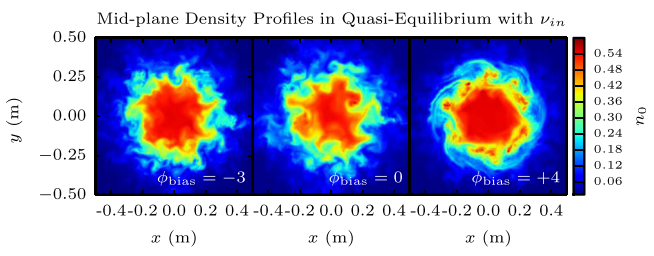

FIG. 10. Comparison of midplane density profiles between biasing runs. Colorbar uses GBS normalized units.

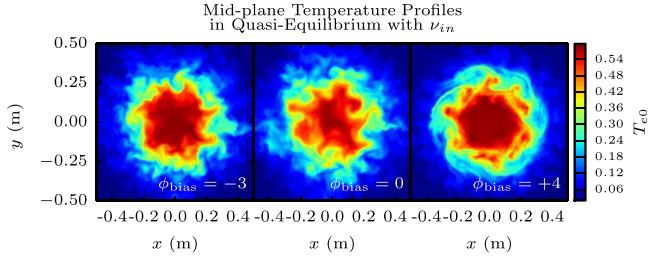

FIG. 11. Comparison of midplane temperature profiles between biasing runs. Colorbar uses GBS normalized units.

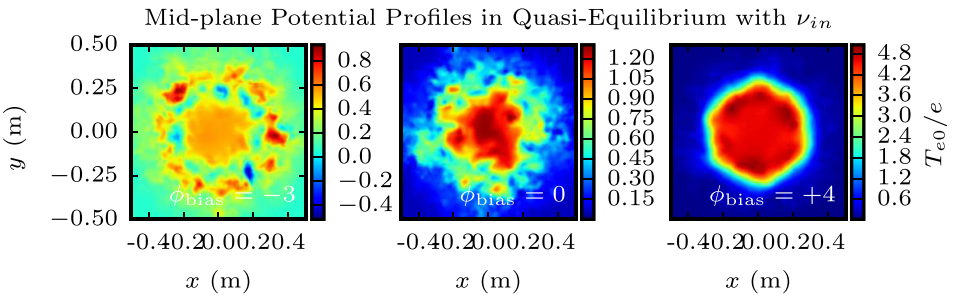

FIG. 12. Comparison of midplane potential profiles between biasing runs. Colorbar uses GBS normalized units.

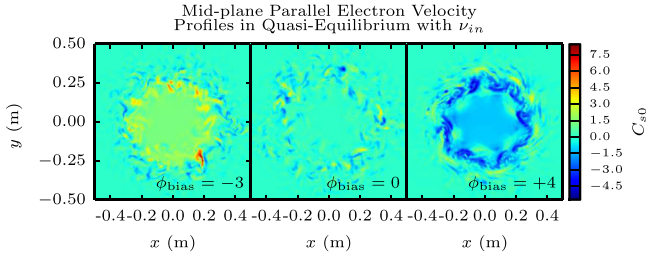

FIG. 13. Comparison of midplane parallel electron velocity profiles between biasing runs. Colorbar uses GBS normalized units.

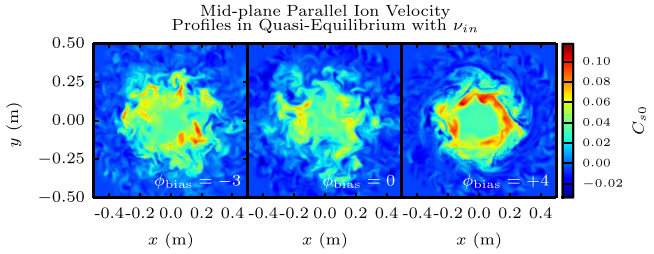

FIG. 14. Comparison of midplane parallel ion velocity profiles between biasing runs. Colorbar uses GBS normalized units.

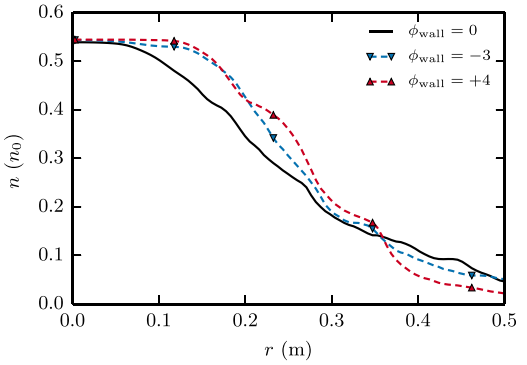

FIG. 16. Time averaged radial plasma density for various single limiter wall biasing runs.

outside the cathode and beyond. The spectral analysis is consistent with the reduced, inward-shifted peak in the fluctuations at negative bias, and at positive bias shows a strong, narrow signal at the rotation frequency of the quasi-coherent mode. An overall steepening and narrowing of the profiles is

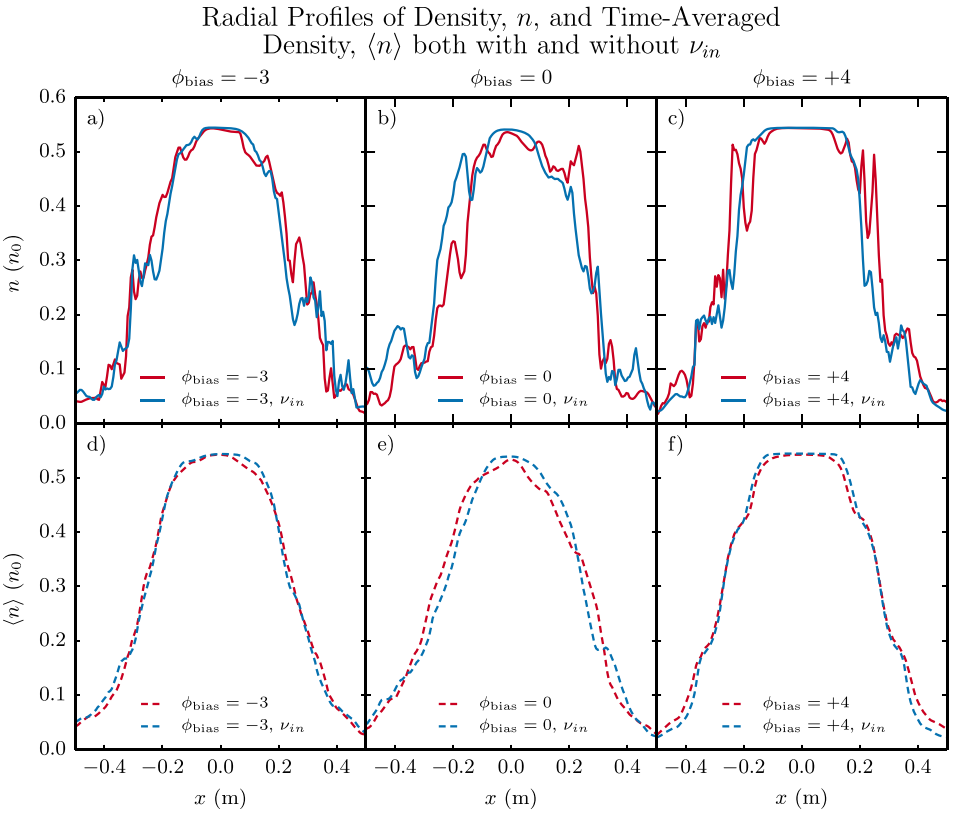

FIG. 15. Midplane density profiles comparing biasing runs (left and right columns) to the unbiased low-flow regime (center column). Total density profiles are shown in the top row, while time-averaged equilibrium quantities are shown in the bottom row.

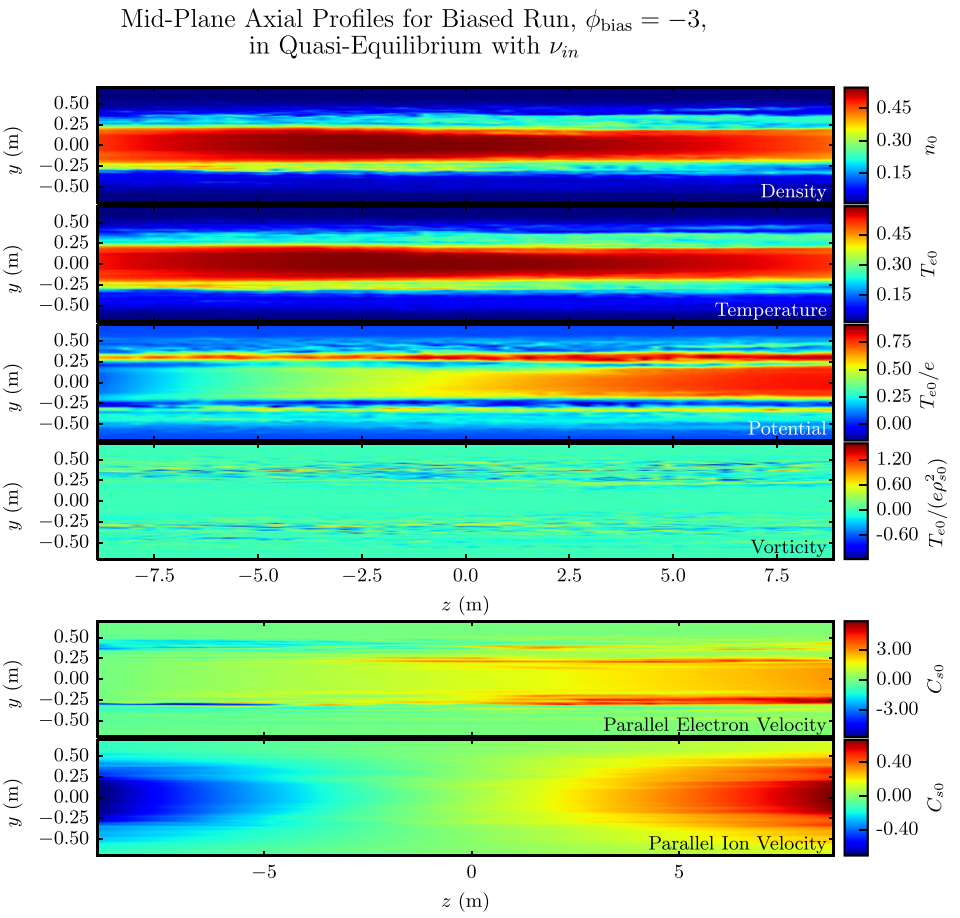

FIG. 17. Midplane on-axis profiles of the density, temperature, potential, vorticity, and parallel electron and ion velocities for $\phi_{\text{bias}} = -3$.

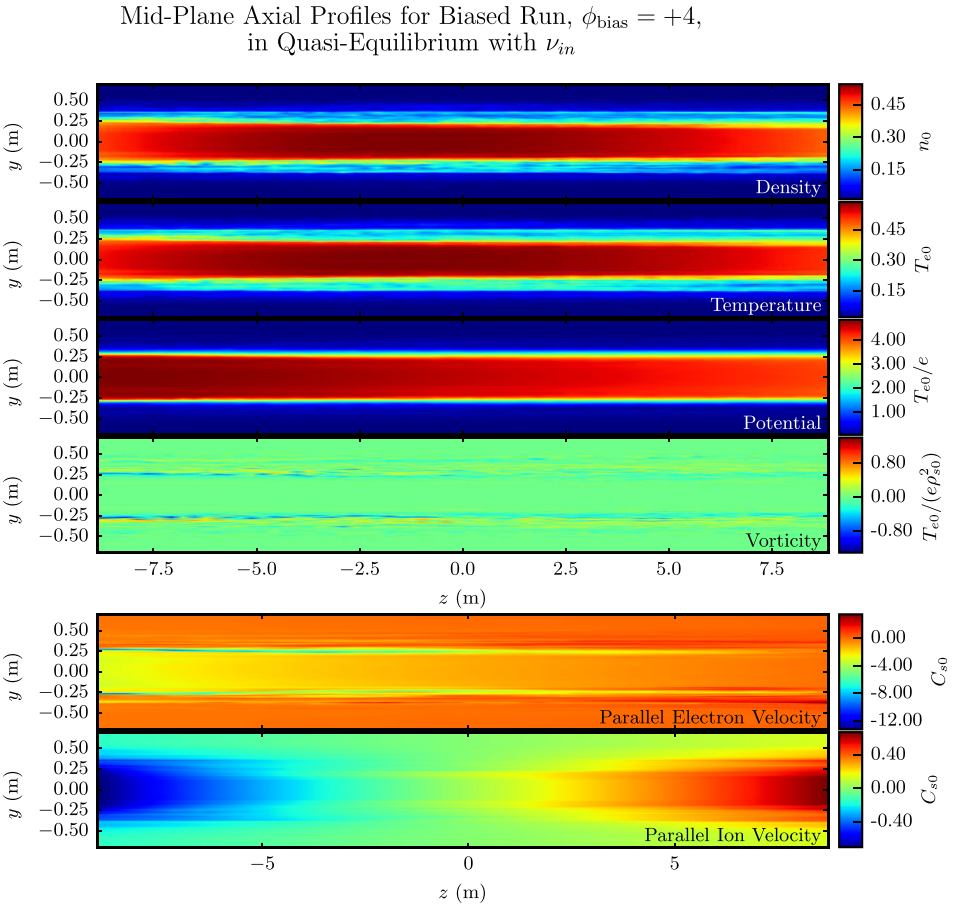

FIG. 18. Midplane on-axis profiles of the density, temperature, potential, vorticity, and parallel electron and ion velocities for $\phi_{\text{bias}} = +4$.

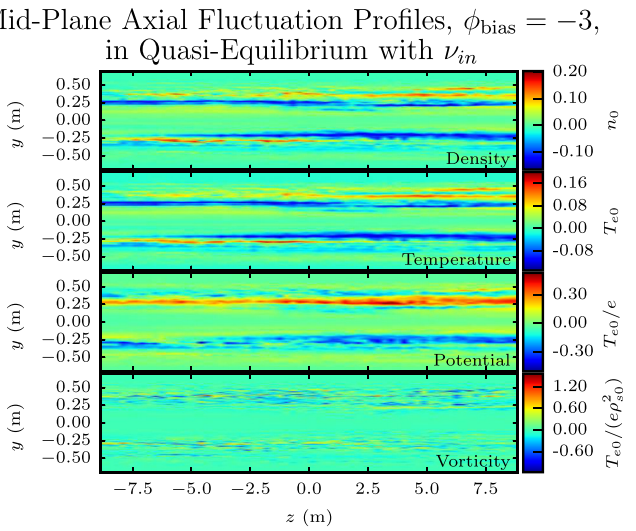

FIG. 19. Midplane axial fluctuation profiles of the density, temperature, and potential for $\phi_{\rm bias} = -3$.

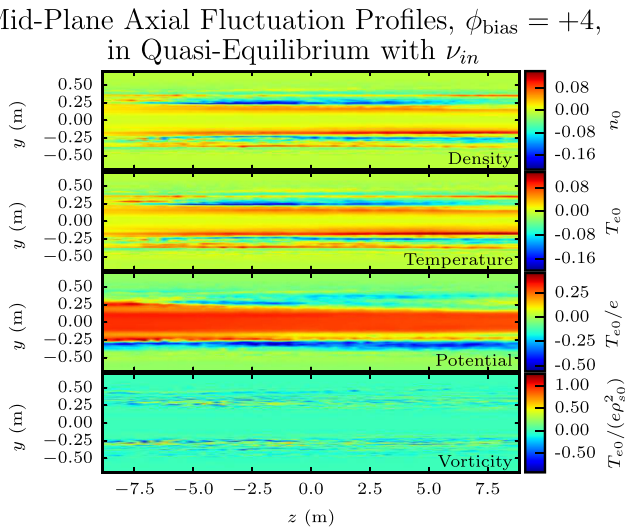

FIG. 20. Midplane axial fluctuation profiles of the density, temperature, and potential for $\phi_{\rm bias} = +4$.

also seen, particularly in the positive case, indicative of the radial narrowing of unstable activity in the biased runs.

Fig. 22 shows the 2D cross-field correlation function of the density fluctuations referenced to a point near the cathode edge. Simulations show radial correlation lengths of about 6 cm in the negatively biased case and 5 cm in the positively biased case, both similar to the unbiased simulation. These are comparable to the profile scale lengths as one would expect for KH modes, and substantially larger (by about a factor of five) than the characteristic driftwave scale $k_\perp \rho_s \sim 1$. The azimuthal correlation lengths in the biased runs, on the other hand, are significantly elongated, consistent with a poloidal stretching of unstable mode structure by the imposed $E \times B$ shear near the cathode edge.

Fig. 23 shows the radial density flux in the three cases. The bias reduces the fluxes at radii several centimeters inside the cathode edge and narrows the radial zone of transport. In the positively biased case, it is noteworthy that, despite a large increase the $E \times B$ shear—something one would expect to further destabilize KH modes—the density flux at its highest is no larger than that in the unbiased run, and radially narrower. Again the conclusion is that increased $E \times B$ shear can reduce, or at least not substantially enhance, the transport of plasma, even though it may locally intensify KH activity.

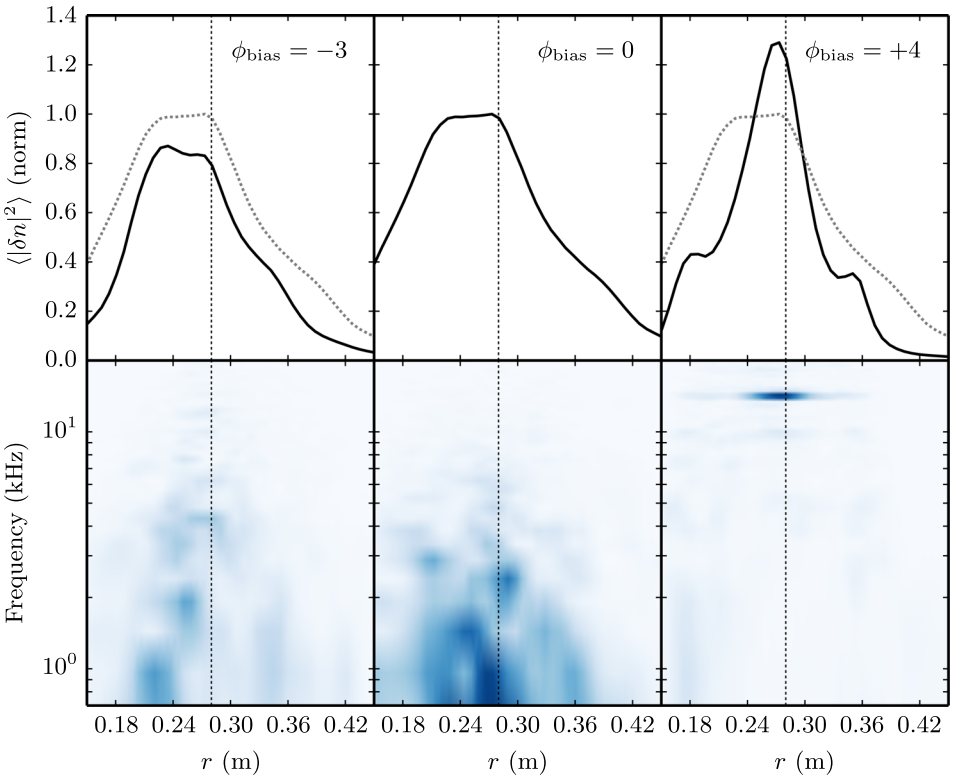

FIG. 21. Radial midplane cuts of density fluctuations and corresponding spectral power density taken over 2 ms. Vertical dotted lines mark the edge of the cathode and dotted lines in the top row mirror the center unbiased case for comparison.

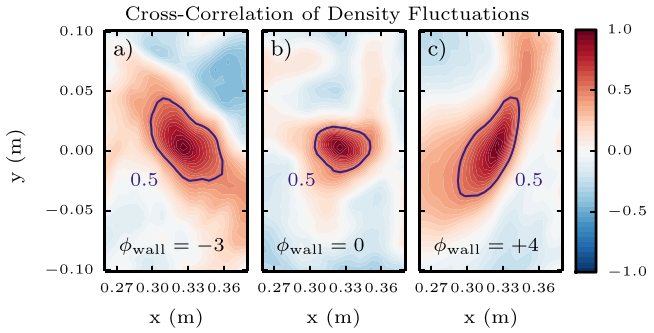

FIG. 22. Cross-correlation map of midplane density fluctuations. The data are correlated with a reference point near the cathode edge. A solid line marks the correlation at 0.5 below the maximum value to give a correlation length.

Or put another way, KH modes are relatively ineffective at transporting plasma across an imposed layer of $E \times B$ shear.

To test whether KH modes are the main driver of fluctuations in the biased runs, Figure 24 shows the steady-state phase of 3D biased simulations in which KH modes have been eliminated by poloidally averaging the nonlinear convective term $[\phi, \omega]$ on the right side of the vorticity equation. No unstable activity arises at all in the positively biased case, while the negatively biased run—perhaps due to its weaker $E \times B$ shear—exhibits small-scale driftwave instability. The steepness of the density profile in the negative case is indicative of weak radial transport by these finite-$k_\parallel$ modes.

Double-wall biasing runs along with 2D simulations are also instructive in exploring fluctuation dynamics. Figs. 25 and 26 show midplane cuts of the density, temperature, and potential in 3D simulations that bias both ends equally, the first positively with $\phi_{wall} = +4$ and the second negatively with $\phi_{wall} = -3$. Figs. 27 and 28 show corresponding simulations of the 2D model given by Eqs. (9)–(11). The purpose of these simulations in the positive case is to test the role of the axial variation and finite $k_\parallel$ modes in the single-wall positively biased run, visible, for example, in Fig. 9. The purpose in the negatively biased case is different: as shown by Fig. 6, for the reasons explained earlier, the plasma potential in the single and double wall biased simulations is strongly different, the latter achieving a full reversal of the flow in the electron diamagnetic direction. This case is nevertheless of

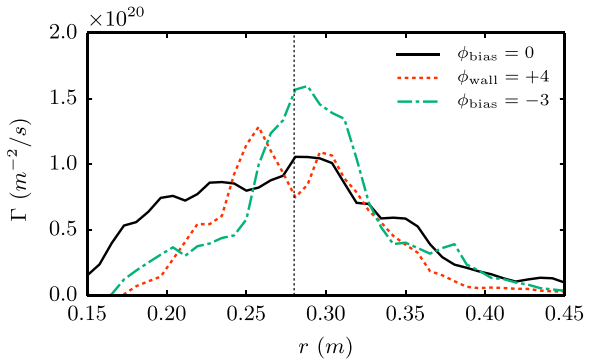

FIG. 23. Radial particle flux as a function of radius. Dashed vertical line marks the edge of the cathode.

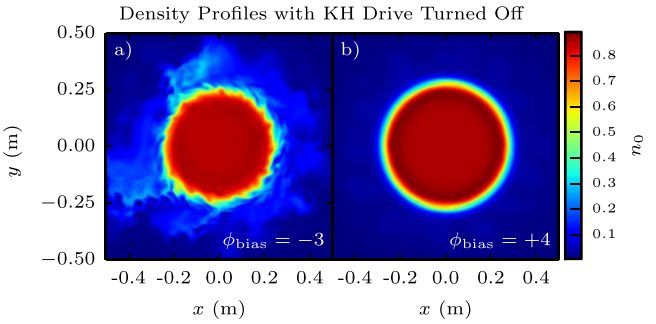

FIG. 24. Midplane density profiles in runs where shear-driven KH turbulence has been suppressed through poloidally averaging the nonlinear convective term, $[\phi, \omega]$, in the vorticity equation.

interest as a further exploration of KH driven transport in a strongly driven system, this time with a narrow sheared layer in the electron diamagnetic direction. Since our model equations and boundary conditions are not invariant under the transformation $\phi \to -\phi$, it is *a priori* unclear how the negatively and positively biased systems will compare.

The comparison of the single wall negatively biased results shown in Figs. 10–12 to the corresponding 3D double wall biased run in Fig. 25 and its 2D analogue in Fig. 27 shows that coherent KH modes with $m \sim 5 - 6$ emerge in all three cases. Further, the steepness of the density and temperature profiles across the $E \times B$ sheared layer again suggests that despite the presence of KH activity, $E \times B$ shear remains an effective means of plasma confinement. Based on the linear theory, one would expect the most unstable poloidal mode number m to be proportional to $\partial_r V_{E\theta} \propto \Delta\phi/\delta^2$. Figure 29 compares the time-averaged radial potential profiles for $\phi_{wall} = +4$ in the single limiter biasing runs, the double wall biasing runs, and the 2D runs. Following, for example, the calculations of Rogers and Dorland,[18] we then fit the profiles to a hyperbolic tangent profile

$$\phi(x) = V_{E0}\delta \tanh\left(\frac{x}{\delta}\right), \tag{15}$$

which has its most unstable linear mode for

$$k_\theta \delta = 0.9, \tag{16}$$

where

$$k_\theta = \exp(im\theta) = \exp(ik_\theta r\theta). \tag{17}$$

The m-value for the fastest growing linear KH mode is therefore

$$m_{max} = k_\theta r_{max} = 0.9\frac{r_{max}}{\delta}, \tag{18}$$

where r_{max} is the radius at which the steepest gradient of ϕ occurs ($x = 0$) according to the potential profile in Eq. (15). Using the fits of the equilibrium potential profiles shown in Figure 29 the fastest growing linear KH mode for the single wall limiter biasing with $\phi_{wall} = +4$ is $m \sim 5$. The double wall bias and the 2D model both give a fastest growing linear mode of $m \sim 4$. The modes actually seen in the simulations are an $m \sim 6$ mode in the single limiter biasing runs and an

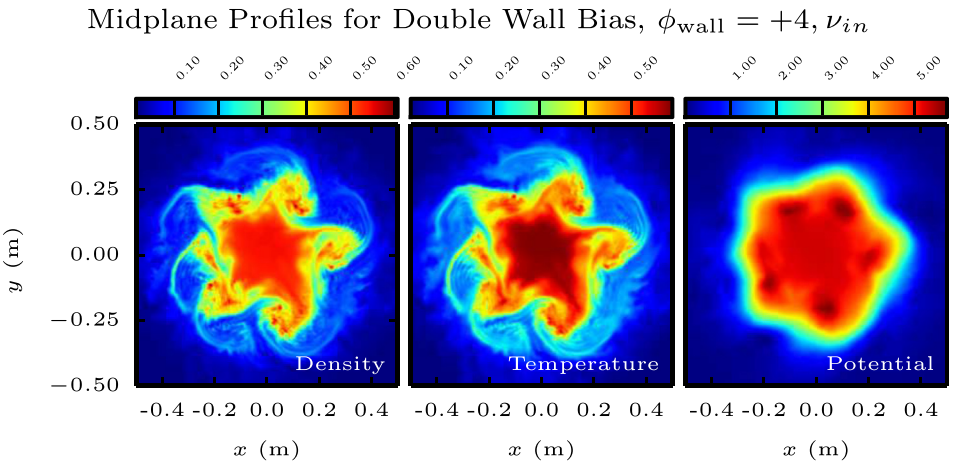

FIG. 25. Midplane plasma profiles of the density, temperature, and potential under front and back wall positive biasing with $\phi_{\rm wall} = +4$. Colorbar values are in GBS normalized units.

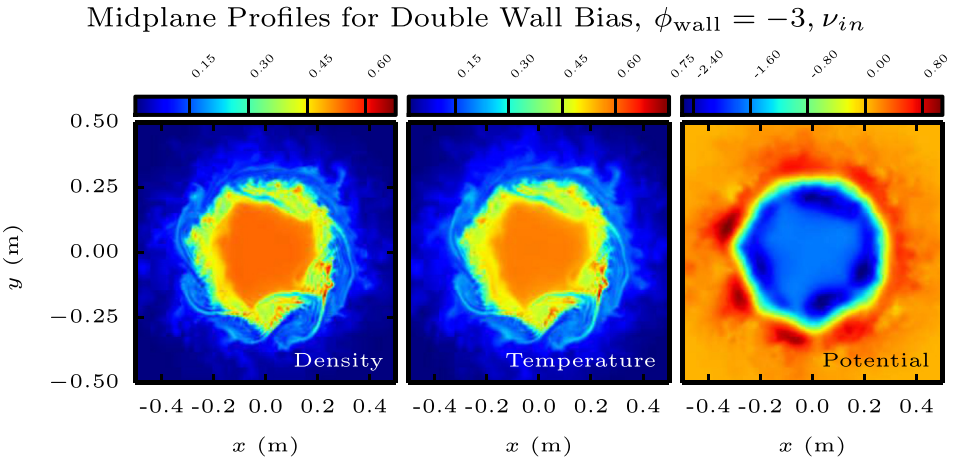

FIG. 26. Midplane plasma profiles of the density, temperature, and potential under front and back wall negative biasing with $\phi_{\rm wall} = -3$. Colorbar values are in GBS normalized units.

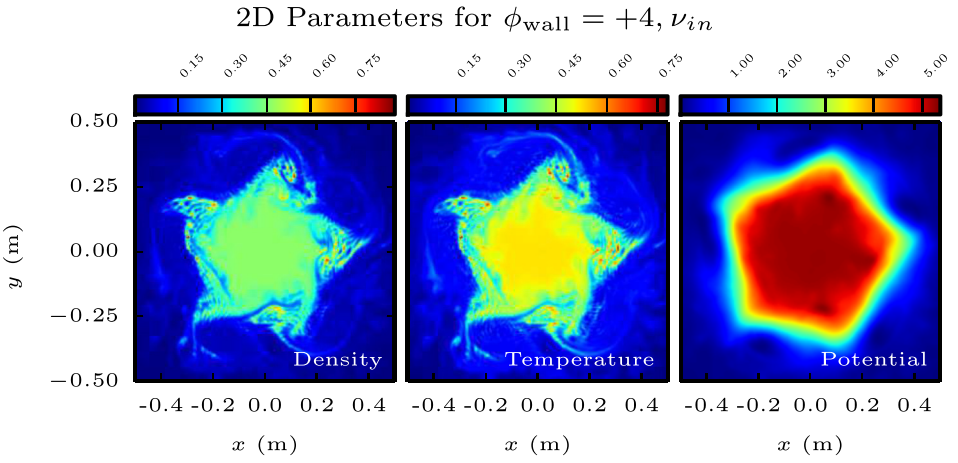

FIG. 27. Plasma density, temperature, and potential profiles for 2D biasing run with $\phi_{\rm wall} = +4$. Colorbar values are in GBS normalized units.

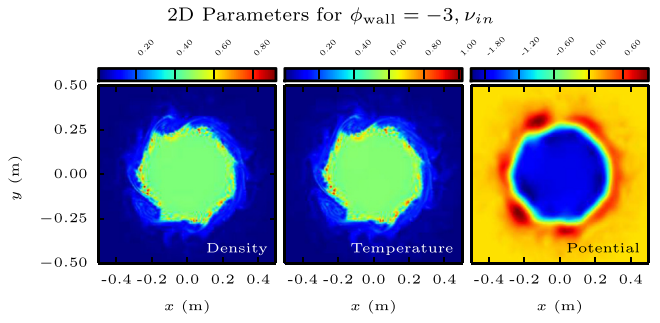

FIG. 28. Plasma density, temperature, and potential profiles for 2D biasing run with $\phi_{\rm wall} = -3$. Colorbar values are in GBS normalized units.

$m \sim 5$ mode in both the 2D and double biasing runs. It is of course uncertain that the dominant linear and nonlinear modes should coincide. But one possible reason for the differences is that the sheath terms are stabilizing to KH, especially at low $k_\perp$. In the analytically tractable limit of a vortex sheet $\partial_r \phi \propto V_{E0}\Theta(r - r_{\rm max})$ one obtains at sufficiently large $k_\perp$:

$$\gamma = k_\perp V_{E0} - \frac{\sigma}{4k_\perp^2 \rho_s^2}\frac{c_s}{R}, \tag{19}$$

where $\sigma = 1.5R/L_z \simeq 0.04$ enters the calculation through the sheath terms in the 2D model discussed earlier. The sheath terms thus become strongly stabilizing at lower $k_\perp$ and may

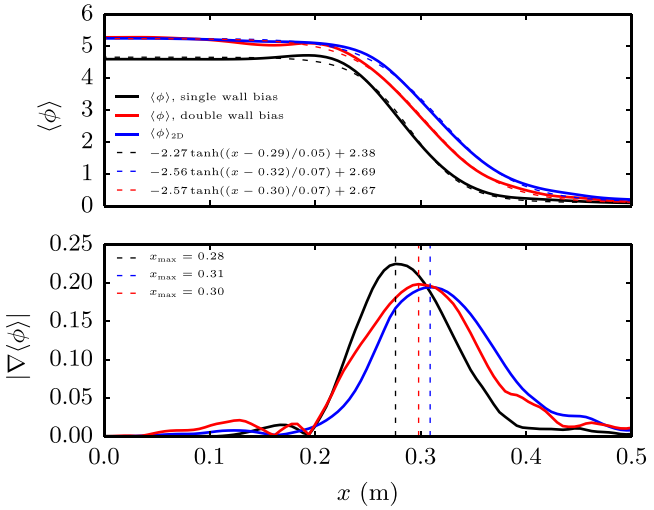

FIG. 29. Comparison of time-averaged $\phi_{wall} = +4$ midplane potential profiles (top) along with corresponding gradient profiles to mark positions of minimum gradient scale lengths (bottom).

push the most unstable mode to higher values than those calculated in Ref. 18.

The 3D double wall negatively biased run in Fig. 26 and its 2D analogue in Fig. 28 show similar but less coherent saturated KH activity, seemingly a mixture of $m = 6\pm1$. A notable feature is the steepness of the profiles, again suggesting the relative inefficacy of the saturated KH modes to produce plasma transport across the imposed $E \times B$ sheared layer.

As a final point, we examine the cross-phase of δn and δE_θ for the single-wall biasing case, which has been of importance in some previous LAPD turbulence work.[6] Spectral analysis of the density fluctuations and poloidal field fluctuations follows the polychromatic spectral techniques outlined by Powers.[19] The cross-power spectrum can then be defined as

$$P_{\delta n \delta E_\theta}(\omega) = F^*_{\delta n}(\omega) F_{\delta E_\theta}(\omega), \tag{20}$$

where F is the Fourier transform of the signal fluctuations, and the asterisk denotes a complex conjugation of the signal. The co-spectrum and quad-spectrum can then be extracted, respectively, as

$$P_{\delta n \delta E_\theta}(\omega) = C_{\delta n \delta E_\theta}(\omega) + iQ_{\delta n \delta E_\theta}(\omega), \tag{21}$$

where i denotes the complex imaginary unit. As in an Argand diagram, the phase of the cross-power spectrum can be calculated as

$$\theta_{\delta n \delta E_\theta}(\omega) = \arctan\left(\frac{Q_{\delta n \delta E_\theta}}{C_{\delta n \delta E_\theta}}\right), \tag{22}$$

where $\theta_{\delta n \delta E_\theta}(\omega)$ is often referred to as the cross-phase spectrum.

Cross-phase maps for the biased runs are shown in Figs. 30 and 31 as a function of both spectral power density and machine radius. The cross-phase is represented as the cosine of the angle so that a value of $+1$ corresponds to the fluctuations being perfectly in phase, while a value of -1 means

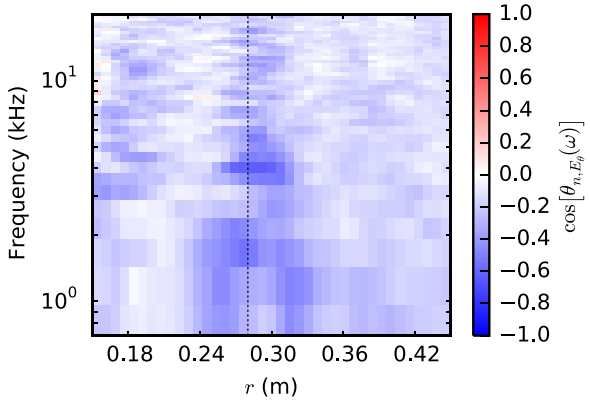

FIG. 30. Cross phase map of negative bias. Vertical dotted line represents the limiter/cathode edge.

they are perfectly out of phase. The cross-phase dynamics for the positively biased runs just outside of the cathode edge shows a streak of frequencies in which the density and poloidal electric field fluctuations are in phase. However, while this differs from that of the negatively biased case in appearance, the relative spectral power of the fluctuations at those radii is negligible for the frequencies seen. The cross-phase therefore seems, in agreement with Schaffner *et al.*,[8] unsuggestive in our simulations.

IV. CONCLUSIONS

We present biasing simulations of the Large Plasma Device (LAPD) using a global, three-dimensional, two-fluid model that applies Bohm sheath boundary conditions at the two end walls perpendicular to the magnetic field and source terms in the density, temperature, and vorticity equations that model the ionization of the LAPD plasma through injection at one end of electrons by the cathode-anode. The external biasing is applied in the LAPD discharges we model through an annular ring just outside the cathode edge that can be biased relative to both the anode and the chamber walls. We simplify this arrangement in the simulations by applying just a single top-hat shaped bias voltage spanning the circular cathode-anode region relative to assumed grounded conditions elsewhere. The applied bias in the simulations can produce a radially sheared jet of plasma with

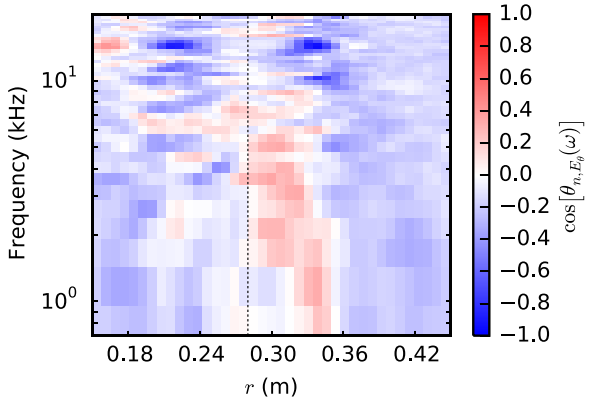

FIG. 31. Cross phase map of positive bias. Vertical dotted line represents the limiter/cathode edge.

given $\Delta\phi \propto V_{E\theta}\delta$ where $\Delta\phi$ is the bias voltage and $V_{E\theta}$ and δ are the average velocity and radial width of the jet. The width δ is governed in the simulations of all biasing regimes by Kelvin-Helmholtz (KH) driven transport across the sheared layer, with weaker transport leading to narrower layers and larger $V_{E\theta}$. The radial transport of plasma by KH modes in the simulations is weaker than one might expect, in the sense that an increase in the applied voltage does not lead to a correspondingly significant increase in the transport and δ, which instead approximately remain the same or decrease overall.

In our numerical experiments, the application of positive biasing, which reinforces the rotation of the unbiased plasma in the ion diamagnetic direction, leads to stronger $E \times B$ flows and a quasi-coherent KH mode with a poloidal mode number $m \simeq 6$, while producing comparable or somewhat reduced plasma transport across the sheared flow layer relative to the unbiased case. On the other hand, the simulations show that the application of negative biasing to the anode end wall alone, with the opposite wall grounded, fails to significantly reverse the flow. This is due to the inability of one-wall negative biasing below roughly $-3T_e/e$ to significantly impact the plasma potential in the presence of a grounded far-end wall. This can be overcome in the simulations by biasing both end walls negatively. This produces a strong $E \times B$ flow layer in the electron diamagnetic direction, saturated KH activity, and steeper profiles, again suggesting that the rotating, saturated KH vortical structures caused by a strongly imposed bias are a relatively ineffective means of plasma transport.

ACKNOWLEDGMENTS

This work was supported by the Center for Computation and Analysis of Reconnection and Turbulence (CICART) under the auspices of the U.S. Department of Energy Experimental Program to Stimulate Competitive Research (EPSCoR) and DOE Grant No. DE-FG02-10ER46372. The authors would like to generously thank Troy A. Carter at UCLA for his discussions and insights concerning LAPD as well as Paolo Ricci at EPFL in Switzerland for the support and use of his Global Braginskii Solver code (GBS).

[1]W. Gekelman, H. Pfister, Z. Lucky, J. Bamber, D. Leneman, and J. Maggs, "Design, construction, and properties of the large plasma research device: The LAPD at UCLA," Rev. Sci. Instrum. **62**(12), 2875–2883 (1991).
[2]D. A. Schaffner, T. A. Carter, G. D. Rossi, D. S. Guice, J. E. Maggs, S. Vincena, and B. Friedman, "Modification of turbulent transport with continuous variation of flow shear in the large plasma device," Phys. Rev. Lett. **109**, 135002 (2012).
[3]W. Horton, J. C. Perez, T. Carter, and R. Bengtson, "Vorticity probes and the characterization of vortices in the Kelvin Helmholtz instability in the large plasma device experiment," Phys. Plasmas **12**(2), 22303 (2005).
[4]J. C. Perez, W. Horton, R. D. Bengtson, and T. Carter, "Study of strong cross-field sheared flow with the vorticity probe in the large plasma devicea)," Phys. Plasmas **13**(5), 055701 (2006).
[5]J. E. Maggs, T. A. Carter, and R. J. Taylor, "Transition from Bohm to classical diffusion due to edge rotation of a cylindrical plasma," Phys. Plasmas **14**(5), 052507 (2007).
[6]T. A. Carter and J. E. Maggs, "Modifications of turbulence and turbulent transport associated with a bias-induced confinement transition in the large plasma device," Phys. Plasmas **16**(1), 012304 (2009).
[7]S. Zhou, W. W. Heidbrink, H. Boehmer, R. McWilliams, T. A. Carter, S. Vincena, B. Friedman, and D. Schaffner, "Sheared-flow induced confinement transition in a linear magnetized plasma," Phys. Plasmas **19**(1), 012116 (2012).
[8]D. A. Schaffner, T. A. Carter, G. D. Rossi, D. S. Guice, J. E. Maggs, S. Vincena, and B. Friedman, "Turbulence and transport suppression scaling with flow shear on the large plasma devicea," Phys. Plasmas **20**(5), 055907 (2013).
[9]B. N. Rogers and P. Ricci, "Low-frequency turbulence in a linear magnetized plasma," Phys. Rev. Lett. **104**, 225002 (2010).
[10]P. Popovich, M. V. Umansky, T. A. Carter, and B. Friedman, "Analysis of plasma instabilities and verification of the BOUT code for the large plasma device," Phys. Plasmas **17**, 102107 (2010).
[11]P. Popovich, M. V. Umansky, T. A. Carter, and B. Friedman, "Modeling of plasma turbulence and transport in the large plasma device," Phys. Plasmas **17**, 122312 (2010).
[12]B. Friedman, T. A. Carter, M. V. Umansky, D. Schaffner, and B. Dudson, "Energy dynamics in a simulation of LAPD turbulence," Phys. Plasmas **19**, 102307 (2012).
[13]B. Friedman, T. A. Carter, M. V. Umansky, D. Schaffner, and I. Joseph, "Nonlinear instability in simulations of large plasma device turbulence," Phys. Plasmas **20**, 055704 (2013).
[14]D. M. Fisher, B. N. Rogers, G. D. Rossi, D. S. Guice, and T. A. Carter, "Three-dimensional two-fluid Braginskii simulations of the large plasma device," Phys. Plasmas **22**(9), 119901 (2015).
[15]A. Zeiler, J. F. Drake, and B. Rogers, "Nonlinear reduced Braginskii equations with ion thermal dynamics in toroidal plasma," Phys. Plasmas **4**, 2134 (1997).
[16]M. B. Thompson, "A comparison of methods for computing autocorrelation time," e-print arXiv:1011.0175[stat.CO].
[17]G. R. Tynan, M. J. Burin, C. Holland, G. Antar, N. Crocker, and P. H. Diamond, "Radially sheared azimuthal flows and turbulent transport in a cylindrical plasma," Phys. Plasmas **11**(11), 5195–5203 (2004).
[18]W. Dorland, F. Jenko, M. Kotschenreuther, and B. N. Rogers, "Electron temperature gradient turbulence," Phys. Rev. Lett. **85**, 5579–5582 (2000).
[19]E. J. Powers, "Spectral techniques for experimental investigation of plasma diffusion due to polychromatic fluctuations," Nucl. Fusion **14**(5), 749 (1974).